Available online at www.sciencedirect.com

SciVerse ScienceDirect

Ceramics International 39 (2013) 3947–3956

CERAMICS INTERNATIONAL

www.elsevier.com/locate/ceramint

Carbon sphere influence on textural properties and bioactivity of mesoporous bioactive glass/hydroxyapatite nanocomposite

Tao Liu[a], Dongzhi Lai[a], Xinxing Feng[b], Hailin Zhu[a], Jianyong Chen[a,*]

[a]*The Key Laboratory of Advanced Textile Materials and Manufacturing Technology, Institute of Materials and Textiles, Zhejiang Sci-Tech University, Hangzhou 310018, PR China*

[b]*The Quartermaster Research Institute of the General Logistics Department of the PLA, Beijing 100082, PR China*

Received 20 August 2012; accepted 22 October 2012
Available online 1 November 2012

Abstract

Mesoporous bioactive glass/hydroxyapatite nanocomposite (MBG-HA) synthesis was conducted through evaporation-induced self-assembly (EISA) method followed by in situ carbonization, with non-ionic block co-polymer as mesoporous template and glucose-derived carbon sphere as co-template. The mixture of different carbon sphere contents into a glass network in the $CaO–SiO_2–P_2O_5$ system tailored the structural, morphological, and textural properties of MBG–HAs. Based on the preliminary results, the carbon sphere content and textural and structural parameters of as synthesized MBG–HAs showed a negative trend. The MBG–HA 0.5 with additional low carbon sphere content, showed a high surface area and large pore volume. The inclusion of HA nanoparticles inside the channels strongly influenced the high carbon sphere content of the MBG–HA8 mesoporous structure. For in vitro bioactivity tests, MBG–HAs with higher textural parameters possessed a faster apatite phase formation kinetics following the sequence MBG–HA0.5 > MBG–HA2 > MBG–HA5 > MBG–HA8.
Crown Copyright © 2012 Published by Elsevier Ltd and Techna Group S.r.l. All rights reserved.

Keywords: A. Sol–gel processes; B. Nanocomposite; D. Apatite; D. Glass

1. Introduction

Since the discovery of 45S5 bioglass by Hench in 1971, various bioactive glasses (BGs) and glass ceramics (BGCs) have been investigated as bone-repair and bone-substitute biomaterials. These bioactive materials can generate an amorphous calcium phosphate layer (ACP) or hydroxyapatite (HA)-type material when exposed to physiological solutions, which is their ability to strongly integrate with live bone [1–5]. Both the chemical composition and textural features of these bioactive materials are important in HA growth. As a result, significant progress has been achieved in the development of improved BGs and the assessment of their bioactive properties [6–11]. In 1991, Li et al. [9] exploited a sol–gel technique to prepare a new family of BGs with improved bioactivity compared with the conventional melt-quenching procedures. The sol–gel method enabled the preparation of glasses at low synthesis temperature and expanded the SiO_2 content in the bioactive composition range by up to 90 mol% [10,11]. Moreover, the method simplified the glass composition and particularly avoided the addition of sodium oxide.

Mesoporous materials have gained attention as potential biomaterials in bone tissue regeneration and drug delivery systems. Currently, studies on mesoporous materials for bone tissue regeneration are conducted by several groups [12–21]. Vallet-Regí [12–14] systematically investigated the in vitro bioactivity of different mesoporous material types, such as MCM-48, SBA-15, MCM-41, and ordered mesoporous bioactive glasses (MBGs), allowing their use in biomedical engineering for tissue regeneration. Zhao et al. prepared a multicomponent MBG ($CaO–SiO_2–P_2O_5$) through the evaporation-induced self-assembly (EISA) method [15–17]. Xia and Chang prepared MBG (M58s)

*Corresponding author. Tel.: +86 571 86843622; fax: +86 571 86843169.
E-mail address: jychen58@yahoo.cn (J. Chen).

0272-8842/$ - see front matter Crown Copyright © 2012 Published by Elsevier Ltd and Techna Group S.r.l. All rights reserved.
http://dx.doi.org/10.1016/j.ceramint.2012.10.242

using a two-step acid-catalyzed self-assembly (TSACSA) method followed by hydrothermal treatment [19–21]. This strategy highlighted the incorporation of structure-directing agents in obtaining successful structures with tunable pore size and internal pore architecture. This method resulted in new-generation MBGs in the ternary $CaO–SiO_2–P_2O_5$ system exhibiting superior bioactivity in vitro, which is attributed to their outstanding surface area and porosity values. These characteristics certainly made BGs highly relevant for drug carriers and bone tissue regeneration.

In mesoscopic scale, MBGs exhibit well-ordered pore arrangement due to the incorporation of a mesoporous template. However, for MBG materials, they exist in an amorphous state due to the amorphous nature of bioglass walls. Processes were explored to prepare mesoporous bioceramics with improved crystalline property similar to the microcrystalline technology-prepared BGCs [22–25]. This progress in MBG modification has fueled research interest to obtain nanocrystalline bioceramics while maintaining the mesostructure. The rapid development of nanotechnology allows advancements in designing a novel silica mesoporous/apatite nanocomposite, where HA nanocrystals are dispersed in noncrystalline silica matrices [26–29]. Furthermore, this nano-sized HA, similar to bone mineral component, has been studied extensively for bone tissue regeneration because of its bioactivity, exceptional biocompatibility, and osteoconductivity. Therefore, an MBG–HA nanocomposite design where the amorphous MBG and nanocrystalline HA combination is dispersed will broaden the functionality beyond the pure material [30,31]. A possible method in preparing bioglass-apatite composite was explored using carbon sphere as the co-template. The role of hydrophilic carbon sphere favored the localized enrichment of calcium ions and facilitated HA nanocrystal formation [30]. However, few studies report the synthesis of this material and consider the influence of carbon sphere content on the mesostructure physiochemical properties and its subsequent in vitro bioactivity. The relation of textural properties (i.e., related to pore volume and size) and apatite nucleation rate are considerably interesting in determining the final properties required for biomedical applications.

The current study demonstrated the MBG–HA nanocomposites in $85SiO_2–10CaO–5P_2O_5$ ternary system through the EISA method followed by in situ carbonization, with non-ionic triblock co-polymer ($EO_{20}PO_{70}EO_{20}$, P123) as template and glucose-derived carbon sphere as co-template. Different from previous reports, the dried gel was initially carbonized for 3 h at 350 °C under Ar atmosphere to stabilize the mesostructure network, and then calcined for 8 h at 700 °C under ambient air to remove the organic template. The effects of carbon sphere content on HA nanoparticle formation in the nanocomposite was studied. Subsequent variation in textural properties, with the addition of carbon sphere content, was observed to expound their influence on the bioactive behavior.

2. Experimental section

2.1. Preparation of carbon sphere

The carbon spheres were prepared by the hydrothermal process described in the literature [32]. Briefly, 8 g glucose were dissolved in water (40 ml) to form a clear solution, which was transferred into a 40 ml teflon-sealed autoclave at 160 °C for 20 h. The black products were collected by centrifugation at 8000 rpm for 10 min, then washed with distilled water and ethanol three times, respectively, and dried at 80 °C for 12 h.

2.2. Synthesis of MBG–HA nanocomposites

According to the method reported by López-Noriega et al. [14], the MBG–HA nanocomposites in the $85SiO_2–10CaO–5P_2O_5$ system were carried out with 4 g of P123, 1 mL of 0.5 N HCl, and 60 g of ethanol. The mixture was stirring at 40 °C in water bath until the solution became clear. Accordingly, 7.4 g of tetraethyl orthosilicate (TEOS), 0.68 g of trithyl phosphate (TEP), 0.98 g of $Ca(NO_3)\cdot 4\,H_2O$ (CaNT), carbon spheres (C) with CaNT at a definite ratio were added into solution. After stirring at 40 °C after 72 h, the resulting sols were cast in Petri dishes (9 cm diameter) to undergo the EISA method at 40 °C. The gelation process occurred after 3 days, and the gels were aged for 7 days in the Petri dishes at 40 °C. Finally, the dried gels were first carbonized at 350 °C under Ar atmosphere for 3 h, and afterwards calcined at 700 °C in air for 8 h. The heating rate for the calcination was controlled at 1 °C/min. According to the weight percent of carbon spheres to the total amount of CaNT, the obtained MBG–HAs with different amount of carbon spheres were denoted as MBG–HA0.5, MBG–HA2, MBG–HA5 and MBG–HA8, respectively (Table 1).

Table 1
Chemical compositions and structural parameters of MBG–HAs with different carbon sphere contents.

Sample	CaNT/(g)	C/(g)	C/CaNT weight ratio	BET surface area/m^2g^{-1}	Pore volume/$cm^3\,g^{-1}$	Pore size/nm
MBG–HA0.5	0.98	0.49	0.5:1	426.1	0.583	5.4
MBG–HA2	0.98	1.96	2:1	376.0	0.539	5.2
MBG–HA5	0.98	4.90	5:1	352.8	0.462	4.9
MBG–HA8	0.98	7.84	8:1	315.2	0.403	4.8

2.3. Assessment of in vitro bioactivity

The in vitro bone-forming bioactivity of MBG–HAs were tested in simulated body fluid (SBF) [33], which has similar composition and ion concentrations to human blood plasma. The weight ratio of MBG–HAs powders to SBF solution volume was 1.5 mg/ml. The samples were immersed into a polythylene bottle without refreshing the SBF solution. After soaking, the powders were collected from SBF by centrifugation, washed with acetone and dried in air.

2.4. Characterization

The surface structure and morphology of MBG–HAs were characterized by field-emission scanning electron microscopy (FESEM; Ultra-55, Carl Zeiss) and fourier transitioned infrared spectroscopy (FTIR; Nicolet 5700, Nicolet USA). Transmission electron microscopy (TEM) images were obtained on a JEOL JEM2100 under a working voltage of 200 kV. Powder X-ray diffraction (XRD) patterns were recorded on a PNAlytical/X'Pert PRO diffractometer using Cu–Ka radiation (40 kV and 40 mA). Nitrogen adsorption and desorption isotherms for all prepared samples were measured at 77 K on a Micromeritics ASAP 2020 system. The specific surface areas and the pore size distributions were calculated from the Brunauer–Emmett–Teller (BET) and Barrett–Joyner–Halenda (BJH) data, respectively.

3. Results and discussion

3.1. Carbon sphere morphology

Fig. 1 shows the TEM and FESEM images of carbon sphere. Fig. 1a shows that the obtained glucose-derived carbon microspheres present spherical and smooth morphology. Previously, various reaction temperature time and raw material concentrations provided carbon microsphere with different sizes [32]. The current study prepared larger carbon microsphere compared with those from Sun. Upon extended reaction time, the carbon microsphere aggregated together under high pressure, with carbon sphere particles size ranging from 100 nm to 300 nm.

3.2. Surface morphologies of MBG–HAs

Fig. 2 shows the surface morphology of MBG–HAs with the addition of carbon sphere using FESEM. After the addition of carbon sphere into the glass matrix, several macropores existed on the surface, with length ranging from 200 nm to 2 μm (Fig. 2), which was attributed to carbon sphere traces left after air calcination. Comparing the images of MBG–HAs with different ratios, the amount of macropores on the glass surface increased along with increasing carbon sphere content. The MBG–HA8 sample exhibited a loose sponge-like morphology with several larger holes on the surface. The larger holes were attributed to the random agglomeration during the synthesis process caused by high carbon sphere content, thereby indirectly increasing the carbon sphere size in the matrix. Therefore, the surface of MBG–HA8 left behind macropores that were larger than the regular size of the carbon sphere after calcination.

3.3. Phase analysis and structural investigations of MBG–HAs

The WAXRD and FTIR techniques proved the nanocrystalline apatite particle formation in the nanocomposite. The powder XRD studies on MBG–HAs samples are shown in Fig. 3. The X-ray diffractograms exhibited the vitreous phase characteristics along with nanocrystalline HA. The obtained MBG–HAs samples showed a broad band at 22°, relative to amorphous silicate, in all WAXRD patterns. Crystalline diffraction peak around $2\theta = 32^\circ$ to 34° appeared after carbon sphere incorporation (Fig. 3(a–d)), suggesting the presence of carbon sphere in facilitating HA crystal formation. The emergence of sharp peak at $2\theta = 26^\circ$ and the corresponding (002) apatite was observed with the increase in carbon sphere content. In addition, the main diffraction (211) peak became narrower and more intense aside from other diffraction peaks (300, 202, 310, 113, 222, 213, 004) that correspond to the apatite reflections, indicating that the crystallinity of the apatite precipitates further

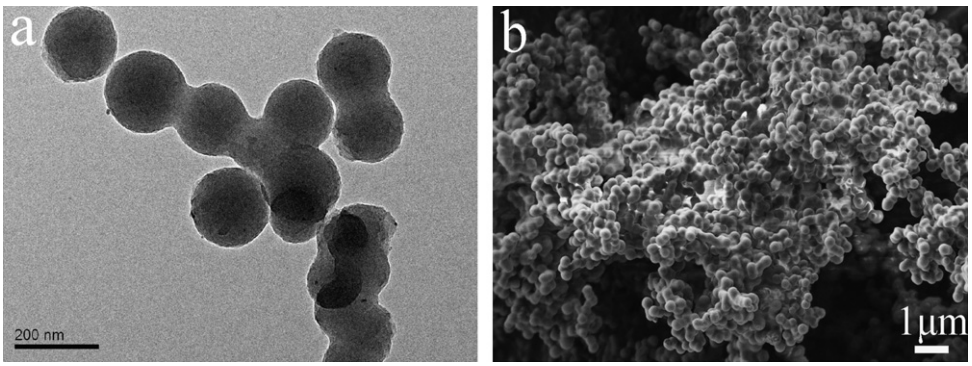

Fig. 1. TEM (a) and FESEM (b) images of carbon spheres.

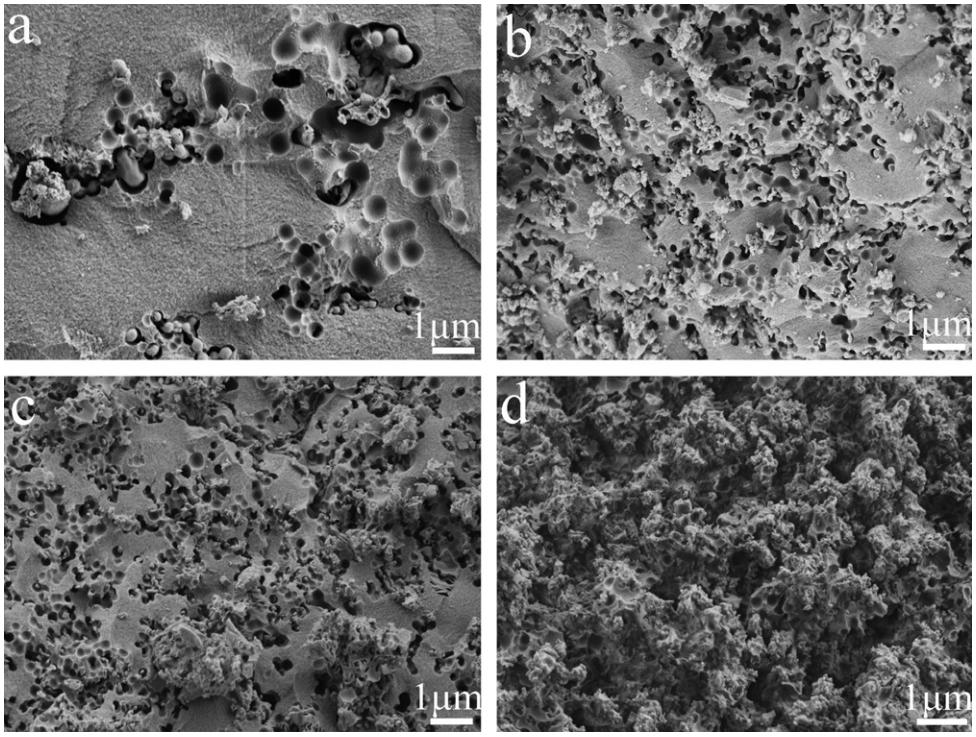

Fig. 2. FESEM micrographs of MBG-HAs: (a) MBG–HA0.5, (b) MBG–HA2, (c) MBG–HA5 and (d) MBG–HA8.

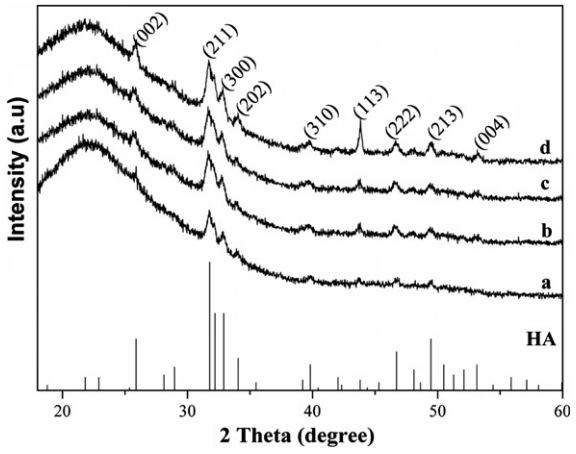

Fig. 3. WAXRD patterns of MBG–HAs, including the standard diffractogram pattern for HA: (a) MBG–HA0.5, (b) MBG–HA2, (c) MBG–HA5 and (d) MBG–HA8.

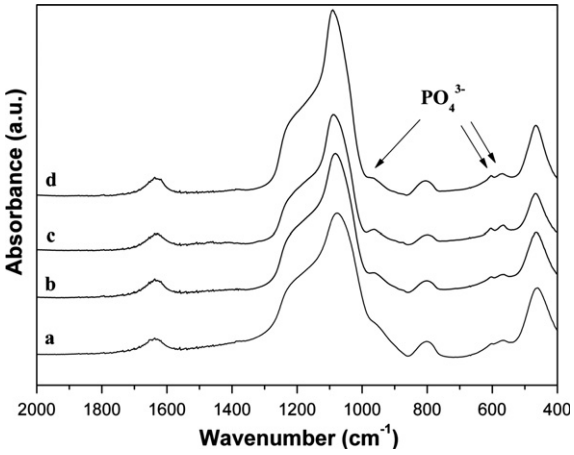

Fig. 4. FTIR spectra of MBG–HAs with different carbon sphere contents: (a) MBG–HA0.5, (b) MBG–HA2, (c) MBG–HA5 and (d) MBG–HA8.

increased with increasing carbon sphere content. A standard pattern (JCPDS 09-0432) was inserted in Fig. 3 to distinguish the HA phase.

Another evidence for the presence of nanocrystals with additional carbon sphere can be obtained from the FTIR spectroscopy. Fig. 4 presents the representative FTIR spectra of MBG–HAs samples. All samples were typically dominated by Si–O–Si asymmetric stretching mode at 1090 cm^{-1}. The Si–O–Si bending vibration was observed around 800 cm^{-1} [34,35], a characteristic of the glass matrix ring structure along with the Si–O–Si rocking mode at 470 cm^{-1}. After carbon sphere incorporation, two obvious bands at 603 and 566 cm^{-1} appeared in the spectra, assigned to the crystalline O–P–O vibrational bands, indicating an apatite-like phase formation [36]. Another characteristic peak of the P–O bands at 965 cm^{-1} was observed. More specifically, the vibrational band intensity at 603 and 566 cm^{-1} increased with increasing carbon sphere content, confirming that carbon sphere incorporation caused an expected HA nanoparticle formation, which was consistent with the WAXRD results.

TEM images directly showed the ordered mesostructure and HA nanocrystals of MBG–HAs (Fig. 5). The MBG–HA

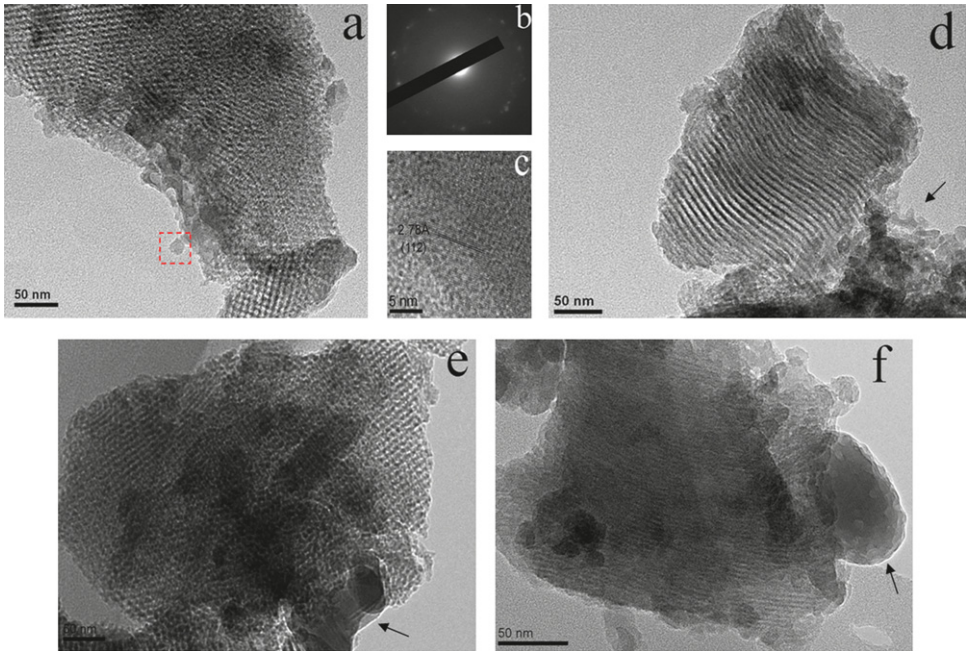

Fig. 5. TEM images of MBG–HAs showing HA nanocrystals around the mesoporous region: (a) MBG–HA0.5, (b) SAED pattern of MBG-HA0.5 material, (c) high-resolution TEM image of the boxed area in (a), showing lattice spacing at 0.278 nm apatite phase, (d) MBG–HA2, (e) MBG–HA5 and (f) MBG–HA8, where the HA nanocrystal is indicated by arrow marks.

samples showed that majority of the HA nanocrystals aggregated outside the mesoporous arrangement (Fig. 5 (a, d–f)). The result differs from the obtained HA nanocrystals reported by Dinesh et al., which were located around the macropores modeled by carbon sphere. At low carbon sphere content, the selected-area electron diffraction (SAED) of MBG–HA0.5 showed a polycrystalline pattern, typical of hydroxyapatite nanocrystals (Fig. 5b). The high-resolution TEM image of MBG–HA0.5 material showed that the HA nanocrystals exhibited a lattice spacing of 0.278 nm, which correspond to the (112) HA reflections (Fig. 5c). However, at high carbon sphere content, majority of the MBG–HA8 sample pore channels were obviously deformed (Fig. 5f), suggesting a distinct mesostructure ordering decrease, which may be attributed with HA material inclusion inside the channels.

The mesostructural properties of calcined MBG–HAs were evaluated by SAXRD (Fig. 6), with N_2 adsorption–desorption characterizations (Fig. 7). The SAXRD patterns of the MBG–HAs materials are shown in Fig. 6. These materials show an apparent diffraction peak around $2\theta = 1.3^{\circ}$, similar to previously reported MBGs and scaffolds [24,25], indicating that all samples after the carbon sphere incorporation have mesoporous pore walls. Diffraction intensities decreased and diffraction peaks gradually broadened with increasing carbon sphere content, suggesting a decreased mesoscopic ordering in the nanocomposite. The MBG–HA8 sample showed that the intensity of (100) reflection was the lowest among all samples, indicating a severe decline in mesoscopic regularity. The diffraction peak positions for the MBG–HAs materials shifted to a higher angle compared with the MBG–HA0.5 material,

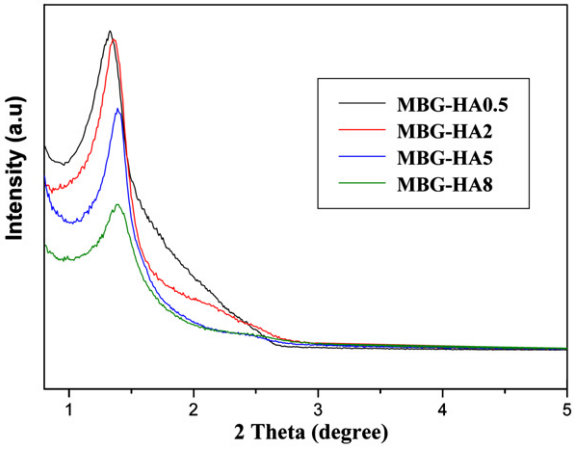

Fig. 6. SAXRD patterns of MBG-HAs after calcination.

which may be attributed to a slight decrease in pore size after carbon sphere incorporation.

Nitrogen sorption isotherms were recorded to access the pore properties of the samples, as shown in Fig. 7. According to the IUPAC classification, all samples exhibit type IV isotherms with type H1 hysteresis loop, which are typical for one-dimensional pore channels having narrow pore size distribution. The data obtained from surface area analysis on nitrogen adsorption/desorption curves are listed in Table 1. The values obtained for the MBG–HAs samples gradually decreased with increasing carbon sphere content. However, the obtained surface area and pore volume were still higher than those from conventional BG samples [37]. The pore size distribution exhibited a slight

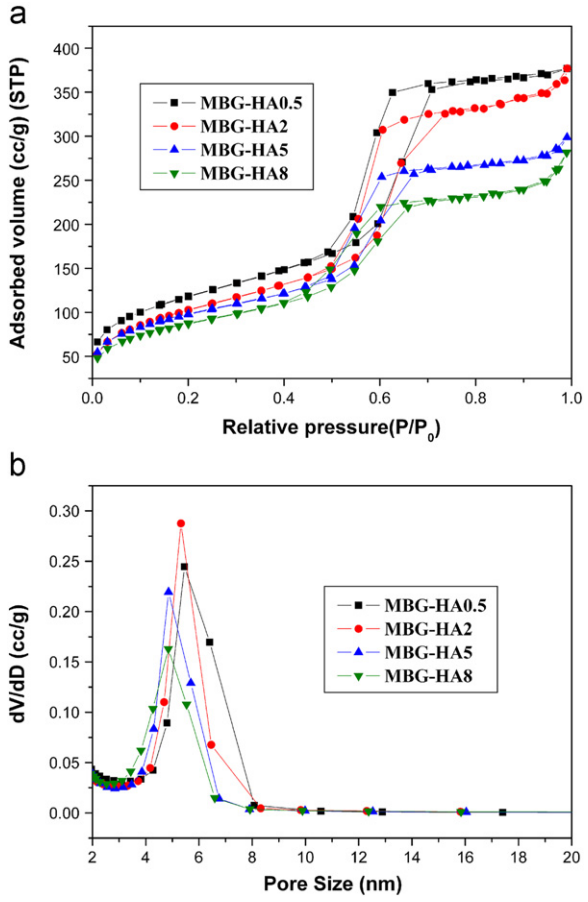

Fig. 7. N_2 adsorption/desorption isotherms (a) and corresponding pore size distribution (b) of MBG–HAs materials.

decrease ranging from 5.4 nm to 4.8 nm, which was consistent with the SAXRD analysis results. Furthermore, the hysteresis width indicated the pore interconnectivity: the wider the hysteresis, the more interconnected pores are [38]. Fig. 7 shows more considerable difference between the hysteresis recorded for MBG–HA samples. MBG–HA8 exhibited narrower hysteresis loops compared with the others, indicating the existence of less interconnected pores.

The XRD, FTIR, SEM, and TEM investigations clearly demonstrated the dependence of the MBG–HA nanocomposite structure on additional carbon sphere amount. Furthermore, the carbon sphere incorporation was conducive to the crystalline HA nanoparticle formation in the glass network. Meanwhile, HA nanocrystals agglomerated and formed clusters with increasing carbon sphere content, resulting in the collapse of glassy network and the destruction of mesopores. This phenomenon can be an occurrence assumed in sample MBG–HA8, which had the highest carbon sphere content. Moreover, their nitrogen sorption capacity decreased with increasing carbon sphere amount, indicating a negative correlation between the carbon sphere amount and the mesostructure (ca. surface area and pore volume). This morphological behavior variation can be caused by the potential presence of HA nanoparticles in the nanocomposite. Therefore, considering the mesostructure and HA nanocrystals, the carbon sphere content should be added in an appropriate range to prepare the ordered MBG–HA nanocomposite using the EISA process.

3.4. In vitro bioactivity assessment

HA formation on MBG–HAs in SBF is an in vitro bioactivity, which is important in assessing the ability to induce bone growth in the human body in vivo. The bone-forming activity of MBG–HAs in vitro was tested in SBF by observing the HA formation on the surface. The MBG–HAs XRD patterns, after SBF soaking for 5 d, are provided in Fig. 8. Compared with the untreated samples in Fig. 3, the samples showed increased contact intensity with SBF for 5 d. From Fig. 8, the intensity of MBG–HAs HA peaks decreased with increasing carbon sphere content, suggesting a slow crystal growth rate in SBF. Furthermore, apatite formation was confirmed by characterizing the SBF soaked samples using FTIR (Fig. 9). After SBF exposure, the other vibrational peaks at approximately 1490, 1440, and 873 cm^{-1} in the MBG–HAs samples after 5 d SBF were associated with the C–O bending mode, indicating a carbonated HA characteristic [36,39]. The appearance of carbonate absorption bands further revealed the bone-forming activity of MBG–HAs in vitro due to the reaction with SBF. By contrast, these sharp peaks detected in a MBG–HA0.5 sample soaked in SBF, the FTIR spectra of MBG–HA8 sample shows weak peaks for similar soaking periods. Furthermore, curve-fitting was done in the O–P–O bending region (530–630 cm^{-1}) to compare the effect of different carbon sphere amounts with the MBG–HAs bioactivity. The curve-fitting results (Fig. 10) showed that all MBG–HAs samples exhibited a weak band (577 cm^{-1}) for amorphous calcium phosphates [40,41], whereas the crystalline phosphates exhibited two distinct bands at 566 and 603 cm^{-1} for O–P–O bending vibrations. The decreased intensity of the

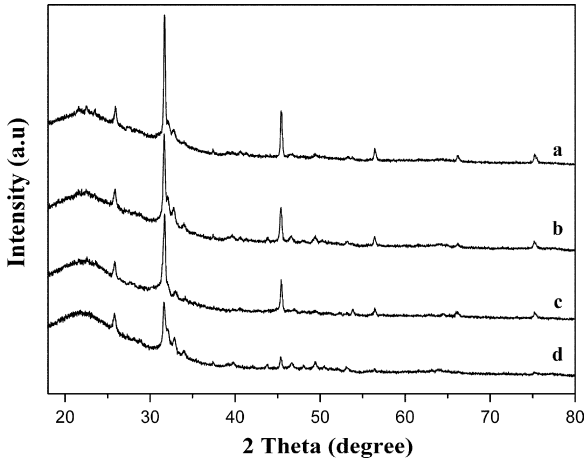

Fig. 8. WAXRD patterns of MBG–HAs soaked in SBF solution for 5 days: (a) MBG–HA0.5, (b) MBG–HA2, (c) MBG–HA5 and (d) MBG–HA8.

crystalline band indicated that the MBG-HAs sample bioactivity decreased with increased carbon sphere content. In the current study, the higher in vitro bioactivity of MBG–HA0.5, with lower carbon sphere content, can be alternatively interpreted through the MBG–HA0.5 material possession of larger pore area and higher pore volumes. Therefore, the samples with superior textural properties exhibited a faster apatite layer nucleation; and these assumptions have been further confirmed by FESEM investigations.

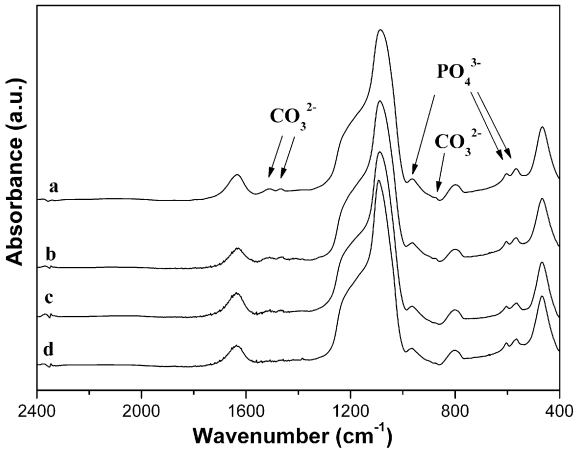

Fig. 9. FTIR spectra of MBG–HAs after immersing in SBF for 5 days: (a) MBG–HA0.5, (b) MBG–HA2, (c) MBG–HA5 and (d) MBG–HA8.

Fig. 11 shows the representative FESEM images of MBG–HAs after soaking in SBF for 5 days. The micrographs revealed that the surface of the nanocomposites exhibited the macropores modeled by carbon spheres and the important changes upon SBF reaction. For the MBG-HA0.5 sample immersed in SBF for 5 d, the HA layer surface was fully covered with denser plate-like crystallites that were packed together, forming a thicker layer. Furthermore, a new phase composed of ball-like particles covering the glass surface can be distinguished. Examining the samples at higher magnification showed that the size of the ball-like crystals ranged from approximately 200 nm to 300 nm in diameter (Fig. 11b). The MBG–HA2 sample surface undergoes a similar process as that of the MBG–HA0.5 sample after immersion in SBF. A layer composed of several spherical particles can be observed covering the glass surface when soaked in SBF for 5 d. Furthermore, agglomerated nanostructured particles formed a dense coating. The plate-like shape crystallites were reduced in number and in size compared with that on MBG–HA0.5 surface after soaking in SBF for 5 d. The high magnification FESEM micrograph showed the size of the spherical crystals at a diameter of approximately 100 nm (Fig. 11d), showing typical apatite morphology.

The surface morphological evolution in MBG–HA5 and MBG–HA8 with SBF reaction was different compared

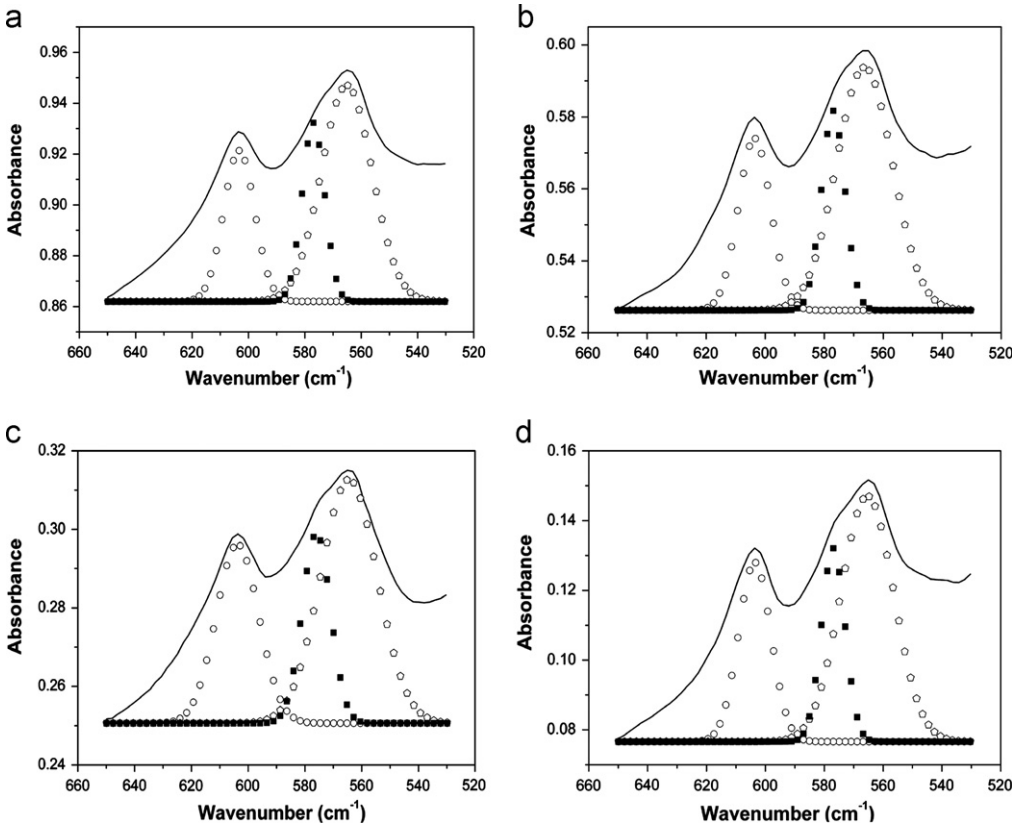

Fig. 10. Curve-fitting results of FTIR spectra of (a) MBG–HA0.5, (b) MBG–HA2, (c) MBG–HA5 and (d) MBG–HA8 after soaking in SBF for 5 days.

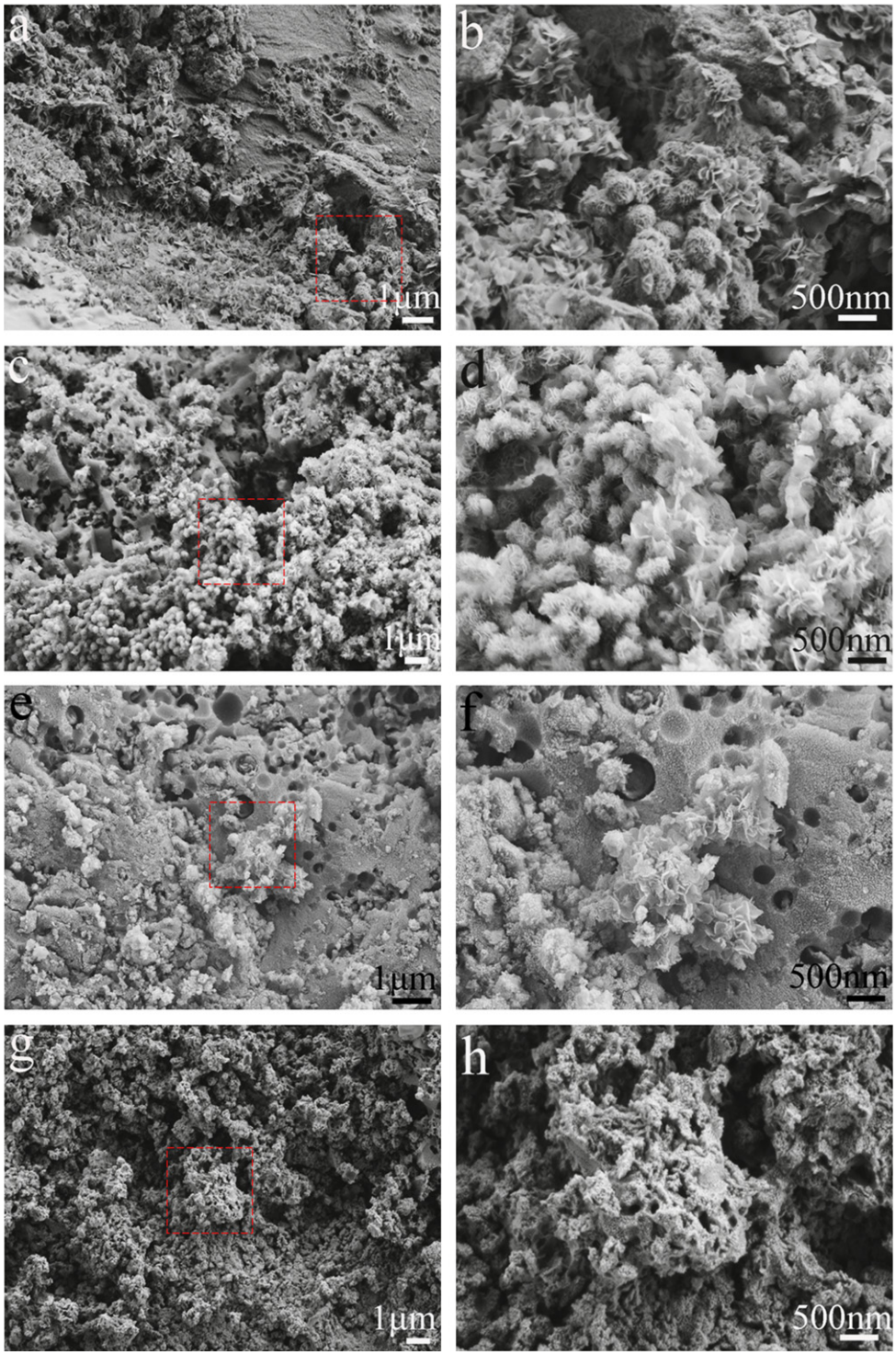

Fig. 11. FESEM images of the MBG–HAs with different chemical compositions after soaking in SBF for 5 days: (a–b), (c–d), (e–f), and (g–h) stands for sample MBG–HA0.5, MBG–HA2, MBG–HA5 and MBG–HA8, respectively.

with that observed from other samples. The MBG–HA5 sample showed small clusters of plate-like crystallites (Fig. 11f). However, the layer toward the plate-shaped crystallites was significantly thinner than those grown on MBG–HA0.5 and MBG–HA2, with the same soaking time. The MBG–HA8 samples showed no morphological changes on their surface even after soaking in SBF for 5 d. Small plate-like crystals were barely observed in Fig. 11h. FESEM results revealed that the bioactivity of MBG–HAs in vitro follows the following sequence: MBG–HA0.5 > MBG–HA2 > MBG–HA5 > MBG–HA8, which agreed with the XRD and FTIR experiments.

The apatite layer formation rate and layer thickness greatly depends on the textural parameters derived from

the mesopores. Therefore, the high surface area and large pore volume are responsible for the enhanced in vitro bioactivity, which agreed with previous reports [17]. The new MBG–HA nanocomposite, MBG–HA0.5, with its larger pore volume and more accessible mesopore surface area, possessed better bone-forming bioactivity in vitro than other MBG–HA materials. This novel nanocomposite, with controllable morphologies has the potential as new biomaterials for drug delivery, implant coating materials, and tissue engineering.

4. Conclusion

Mesoporous bioactive glass/hydroxyapatite nanocomposite was successfully synthesized, with P123 and carbon sphere as cotemplate approach, through the combination of EISA and in situ carbonization method. The presence of carbon sphere was beneficial to HA nanoparticle formation. The partial addition of carbon sphere in the glass framework maintained the mesoporous structure of the pore walls. However, at high carbon sphere content, the mesostructure ordering in MBG–HA8 was greatly influenced by the HA nanocrystal formation. Their physiochemical and biological properties were influenced when mixing different carbon sphere contents. Pore size decreased with increasing carbon sphere content, whereas a concomitant decrease in specific surface area and pore volume was observed. The in vitro bioactivity measurements of these nanocomposites revealed that the lower carbon sphere content in the nanocomposite led to a higher HA layer formation rate in SBF. Furthermore, this synthesis method can be extended to other simple and multicomponent bioactive glass for the production of controlled surface area and pore size distribution with different carbon sphere contents.

Acknowledgments

The authors gratefully acknowledge the financial support of this study by National Natural Science Foundation of China (Grant no: 50973096, 50903073 and 31070867).

References

[1] L.L. Hench, R.J. Splinter, W.C. Allen, T.K. Greenlee, Bonding mechanism at the interface of ceramic prosthetic materials, Journal of Biomedical Materials Research 5 (1971) 117–141.
[2] M. Vallet-Regí, C.V. Ragel, A.J. Salinas, Glasses with medical applications, European Journal of Inorganic Chemistry (2003) (2003) 1029–1042.
[3] L.L. Hench, The story of bioglass®, Journal of Materials Science: Materials in Medicine 17 (2006) 967–978.
[4] T. Kokubo, H. Takadama, How useful is SBF in predicting in vivo bone bioactivity?, Biomaterials 27 (2006) 2907–2915
[5] D. Arcos, I. Izquierdo-Barba, M. Vallet-Regí, Promising trends of bioceramics in the biomaterials field, Journal of Materials Science: Materials in Medicine 20 (2009) 447–455.
[6] T. Kokubo, H. Kushitani, S. Sakka, T. Kitsugi, T. Yamamuro, Solutions able to reproduce in vivo surface-structure changes in bioactive glass-ceramic A-W, Journal of Biomedical Materials Research 24 (1990) 721–734.
[7] T. Kokubo, S. Ito, M. Shigematsu, S. Sakka, T. Yamamuro, Fatigue and life-time of bioactive glass-ceramic A-W containing apatite and wollastonite, Journal of Materials Science 22 (1987) 4067–4070.
[8] W. Vogel, W. Höland, Development, structure, properties and application of glass-ceramics for medicine, Journal of Non-Crystalline Solids 123 (1990) 349–353.
[9] R. Li, A.E. Clark, L.L. Hench, An investigation of bioactive glass powders by sol-gel processing, **Journal** of **Applied Biomaterials** 2 (1991) 231–239.
[10] J.P. Zhong, D.C. Greenspan, Processing and properties of sol–gel bioactive glasses, Journal of Biomedical Materials Research 53 (2000) 694–701.
[11] I. Izquierdo-Barba, L. Ruiz-González, J.C. Doadrio, J.M. González-Calbet, M. Vallet-Regí, Tissue regeneration: a new property of mesoporous materials, Solid State Science 7 (2005) 983–989.
[12] I. Izquierdo-Barba, Á. Martinez, A.L. Doadrio, J. Pérez-Pariente, M. Vallet-Regí, Release evaluation of drugs from ordered three-dimensional silica structures, European Journal of Pharmaceutical Sciences 26 (2005) 365–373.
[13] M. Vallet-Regí, Ordered mesoporous materials in the context of drug delivery systems and bone tissue engineering, Chemistry—A European Journal 12 (2006) 5934–5943.
[14] A. López-Noriega, D. Acros, I. Izquierdo-Barba, Y. Sakamoto, O. Terasaki, M. Vallet-Regí, Ordered mesoporous bioactive glasses for bone tissue regeneration, Chemistry of Materials 18 (2006) 3137–3144.
[15] X.X. Yan, C.Z. Yu, X.F. Zhou, J.W. Tang, D.Y. Zhao, Highly ordered mesoporous bioactive glasses with superior in vitro bone-forming bioactivities, Angewandte Chemie International Edition 43 (2004) 5980–5984.
[16] X.X. Yan, H.X. Deng, X.H. Huang, C.Z. Yu, et al., Mesoporous bioactive glasses. I. Synthesis and structural characterization, Journal of Non-Crystalline Solids 351 (2005) 3209–3217.
[17] X.X. Yan, X.H. Huang, C.Z. Yu, D.Y. Zhao, et al., The in-vitro bioactivity of mesoporous bioactive glasses, Biomaterials 27 (2006) 3396–3403.
[18] Y.F. Zhu, C.T. Wu, Y. Ramaswamy, E. Kockrick, P. Simon, S. Kaskel, H. Zreiqat, Preparation, characterization and in vitro bioactivity of mesoporous bioactive glasses (MBGs) scaffolds for bone tissue engineering, Microporous and Mesoporous Materials 112 (2008) 494–503.
[19] W. Xia, J. Chang, Well-ordered mesoporous bioactive glasses (MBG): a promising bioactive drug delivery system, Journal of Controlled Release 110 (2006) 522–530.
[20] W. Xia, J. Chang, Preparation, in vitro bioactivity and drug release property of well-ordered mesoporous 58S bioactive glass, Journal of Non-Crystalline Solids 354 (2008) 1338–1341.
[21] W. Xia, J. Chang, J.P. Lin, J.Q. Zhu, The pH-controlled dual-drug release from mesoporous bioactive glass/polypeptide graft copolymer nanomicelle composites, European Journal of Pharmaceutics and Biopharmaceutics 69 (2008) 546–552.
[22] Q.H. Shi, J.F. Wang, J.P. Zhang, J. Fan, G.D. Stucky, Rapid-setting, mesoporous, bioactive glass cements that induce accelerated in vitro apatite formation, Advanced Materials 18 (2006) 1038–1042.
[23] X. Li, X.P. Wang, D.N. He, J.L. Shi, Synthesis and characterization of mesoporous CaO–MO–SiO_2–P_2O_5 (M=Mg, Zn, Cu) bioactive glasses/composites, Journal of Materials Chemistry 18 (2008) 4103–4109.
[24] Y.F. Zhu, X.L. Li, J.H. Yang, S.L. Wang, H. Gao, N. Hanagata, Composition–structure–property relationships of the CaO–M_xO_y–SiO_2–P_2O_5 (M=Zr, Mg, Sr) mesoporous bioactive glass (MBG) scaffolds, Journal of Materials Chemistry 21 (2011) 9208–9218.
[25] X.P. Wang, X. Li, S. Ito, Y. Sogo, Synthesis and characterization of hierarchically macroporous and mesoporous CaO–MO–SiO_2–P_2O_5 (M=Mg, Zn, Sr) bioactive glass scaffolds, Acta Biomaterialia 7 (2011) 3638–3644.

[26] J. Andersson, S. Areva, B. Spliethoff, M. Lindén, Sol–gel synthesis of a multifunctional, hierarchically porous silica/apatite composite, Biomaterials 26 (2005) 6827–6835.
[27] A. Díaz, T. López, J. Manjarrez, E. Basaldella, J.A. Odriozola, et al., Growth of hydroxyapatite in a biocompatible mesoporous ordered silica, Acta Biomaterialia 2 (2006) 173–179.
[28] A. Sousa, K.C. Souza, E.M.B. Sousa, Mesoporous silica/apatite nanocomposite: special synthesis route to control local drug delivery, Acta Biomaterialia 4 (2008) 671–679.
[29] A. Borwoka, A. Szczes, Synthesis of a novel silica/apatite mesoporous nanocomposite, Materials Letters 65 (2011) 175–178.
[30] D. Jagadeesan, C. Deepak, K. Siva, M. Eswara-Moorthy, Carbon spheres assisted synthesis of porous bioactive glass containing hydroxycarbonate apatite nanocrystals: a material with high in vitro bioactivity, Journal of Physial Chemistry C 112 (2008) 7379–7384.
[31] M. Cicuéndez, M.T. Portolés, I. Izquierdo-Barba, M. Vallet-Regí, New nanocomposite system with nanocrystalline apatite embedded into mesoporous bioactive glass, Chemistry of Materials 24 (2012) 1100–1106.
[32] X.M. Sun, Y.D. Li, Colloidal carbon spheres and their core/shell structures with noble-metal nanoparticles, Angewandte Chemie International Edition 43 (2004) 597–601.
[33] T. Abe, T. Kokubo, T. Yamamuro, Apatite coating on ceramics, metals and polymers utilizing a biological process, Journal of Materials Science: Materials in Medicine 1 (1990) 233–238.
[34] H. Aguiar, J. Serra, P. Gonzalez, B. Leon, Structural study of sol-gel silicate glasses by IR and Raman spectroscopies, Journal of Non-Crystalline Solids 355 (2009) 475–480.
[35] H. Aguiar, J. Serra, P. Gonzalez, B. Leon, Influence of the stabilization temperature on the structure of bioactive sol-gel silicate glasses, Journal of American Ceramic Society 93 (2010) 2286–2291.
[36] M. Vallet-Regí, A.M. Romero, C.V. Ragel, R.Z. LeGeros, XRD, SEM-EDS, and FTIR studies of in vitro growth of an apatite-like layer on sol–gel glasses, Journal of Biomedical Materials Research 44 (1999) 416–421.
[37] D. Arcos, D.C. Greenspan, M. Vallet-Regí, Influence of the stabilization temperature on textural and structural features and ion release in SiO_2–CaO–P_2O_5 sol–gel glasses, Chemistry of Materials 14 (2002) 1515–1522.
[38] M.T. Colomer, Nanoporous anatase thin films as fast proton-conducting materials, Advanced Materials 18 (2006) 371–374.
[39] C. Vaid, S. Murugavel, R. Kashayap, R.P. Tandon, Synthesis and in vitro bioactivity of surfactant templated mesoporous sodium silicate glasses, Microporous and Mesoporous Materials 159 (2012) 17–23.
[40] H.W. Yan, K. Zhang, C.F. Blanford, L.F. Francis, A. Stein, In vitro hydroxycarbonate apatite mineralization of CaO–SiO_2 sol–gel glasses with a three-dimensionally ordered macroporous structure, Chemistry of Materials 13 (2001) 1374–1382.
[41] D. Arcos, M. Vila, A. López-Noriega, F. Rossignol, E. Champion, M. Vallet-Regí, Mesoporous bioactive glasses: mechanical reinforcement by means of a biomimetic process, Acta Biomaterialia. 7 (2011) 2952-2959.